eprints@whiterose.ac.uk
https://eprints.whiterose.ac.uk/

Selective Imines Synthesis by Designing Atomic-level Cu-Pt Electron Transfer Channel over CdS Nanosheets

*Yue-Hua Li[†], Yin-Feng Wang[†], Jing-Yu Li[†], Ming-Yu Qi[†], Marco Conte[‡], Zi-Rong Tang[†, *], and Yi-Jun Xu[†, *]*

† College of Chemistry, State Key Laboratory of Photocatalysis on Energy and Environment, Fuzhou University, Fuzhou, 350116, China.

‡ Department of Chemistry, University of Sheffield, Sheffield, S3 7HF, UK

KEYWORDS: Cu doping, Pt single atoms, atomic-level electron transfer channel, selective imines synthesis, H_2 evolution

ABSTRACT. The precise design of charge carriers relay channel and active sites of semiconductor-based photocatalysts is highly crucial for target selective photoredox synthesis. In this context, we report an atomic-level catalyst design strategy based on depositing Pt single atoms (SAs) onto Cu-doped ultrathin cadmium sulfide nanosheets (CdS/Cu/Pt) to enable optimized band structure, directional charge transfer channel, and favorable catalytic sites for efficient and selective dehydrocoupling of amines to imines and hydrogen (H_2). The Cu dopant acts as a unique electron bridge to construct a directional Cu-Pt electron transfer channel with the assistance of atomically dispersed Pt sites, thereby promoting the charge separation and transfer kinetics. The introduction of Pt SAs not only facilitates the H_2 generation by decreasing the overpotential of proton reduction, but also improves the selectivity of imines synthesis because the weak adsorption of imines on Pt SAs prevents further hydrogenation of imines to secondary amines. This work is anticipated to inspire further rational design of semiconductor-based photocatalysts with atomic precision for coproduction of renewable fuels and value-added fine chemicals.

1. Introduction

As important building blocks in the synthesis of quinolines, cucurbiturils, and oxaziridines, imines occupy pivotal positions in the commercial manufacture of pharmaceuticals, pesticides, and organic dyes.[1-6] The general synthetic protocols of imines depend on the condensation of amines with aldehydes or ketones, which is accompanied by the release of water. To promote the reaction equilibrium for imines generation, the elevated temperatures and dehydrating agents (i.e., molecular sieves) are adopted, which lead to the unsatisfactory selectivity of targeted imines and late stage product purification.[4,7] In this context, light-driven coupling of primary amines has been regarded as an alternative to the synthesis of imines because of its high efficiency and convenience in the formation of reactive intermediates (i.e., carbon-centered radicals), as well as mild conditions and free emission of pollutants.[8,9] In addition, developing photocatalytic amines dehydrocoupling systems under anaerobic conditions avoids the waste of reduction ability of photoelectrons and unexpected side reactions caused by the utilization of oxygen as the electron acceptor, which provides a straightforward, atom-economic and step-efficient approach for simultaneously accessing C–N coupled imines and green hydrogen (H_2) in one photoredox cycle.[2,10-13]

In terms of constructing efficient and selective dual-functional photoredox systems for the co-production of imines and H_2, cadmium sulfide (CdS) featuring controllable morphology, desirable visible light response, and suitable band edge positions is deemed as a potential candidate.[14-16] However, the photocatalytic activity and selectivity of bare CdS is inevitably restricted by its inherent drawbacks of fast recombination of charge carriers and lack of function-oriented active sites.[17,18] In order to leap over these obstacles, heteroatom doping offers a three-in-one integrated solution to synchronously modulate the light absorption, accelerate the separation and transfer of charge carriers, and increase the catalytic active sites by introducing the dopant-related energy level within the mid-gap region of semiconductor catalysts and thus ameliorating their electronic structure.[19-23] However, the new charge recombination centers are concomitantly introduced by heteroatom doping, which plays a double-edged sword role in the regulation of charge carrier separation kinetics.[24] Therefore, intelligently integrating heteroatom doping with the additional electron-trapping sites to construct multi-level charge transfer channels in semiconductor-based photocatalysts is imperative to further promote their charge carrier separation and transfer kinetics toward efficient photoredox applications.[25,26] Recently, metal single atoms (SAs) cocatalysts with maximum atom-utilization efficiency, superb electron-withdrawing capability, and unsaturated coordination sites have captivated considerable attention in facilitating the charge transfer and regulating the surface reaction of advanced heterogeneous photocatalytic systems.[27-37] In addition, the open and accessible surface of two-dimensional semiconductor nanosheets (NSs) provides a multifunctional platform for the sufficient exposure of active sites and collectively precise design of heteroatom doping and SAs in a controllable way.[23,38-41]

Herein, we report the rational synthesis of atomic-level Cu-Pt electron transfer channel by immobilizing Pt SAs onto heteroatom Cu-doped ultrathin CdS NSs to fabricate ternary CdS/Cu/Pt composite toward integrated photoredox-catalyzed H_2 evolution and dehydrocoupling of amines with high imines selectivity and good substrate tolerance. Such an atomic-level Cu-Pt electron transfer

channel, composed of Cu dopant as a unique electron bridge and Pt SAs as electron-withdrawing sites, is elaborately designed to endow the markedly promoted separation and directional transfer of charge carriers, which therefore contribute to the distinct photoactivity improvement. Because of the decreased overpotential of proton reduction to H_2 and the weak adsorption of imines on Pt, the introduction of Pt SAs as multifunctional reaction centers promotes the C-N coupling kinetics for selective imines production and accompanying H_2 evolution. By virtue of the joint detection of reactive species and intermediates, the underlying addition-elimination mechanism for photocatalytic BA dehydrocoupling has also been unveiled. This work is expected to open a new avenue for simultaneously regulating light absorption, directional electron flow, and catalytic active sites of semiconductor-based catalysts to promote light-driven organic synthesis and accompanying H_2 production in a cooperative manner.

2. Results and Discussion

The CdS/Cu/Pt composites are fabricated *via* a combinatorial procedure (unless otherwise noted, the characterizations are mainly focused on CdS/Cu/0.4Pt, because it exhibits the optimal photoactivity in the subsequent activity tests), as illustrated in **Figure 1a**. Initially, the Cu-doped ultrathin CdS nanosheets (CdS/Cu NSs) are prepared by a facile solvothermal method in a mixture of ethylenediamine and deionized (DI) water using $Cu(CH_3COO)_2 \cdot H_2O$ as the doping precursor.[42,43] As portrayed in the scanning electron microscopy (SEM) and transmission electron microscopy (TEM) images (**Figure S1a-c**), CdS/Cu features flake-like morphology without discernible nanoparticles (NPs), which is the same as that of blank CdS. Atomic force microscopy (AFM) image and related height profiles in **Figure S1d-f** confirm that the thickness of CdS/Cu NSs is *ca.* 3.5 nm. The high-resolution TEM (HRTEM) image (**Figure S1g**) displays lattice spacing of 0.34 and 0.36 nm, indexing to the (002) and (100) crystal facets of CdS.[18] The energy-dispersive X-ray spectro-scopy (EDX) spectrum (**Figure S1h**) and elemental mapping results (**Figure S1i**) demonstrate the coexistence and uniform distribution of Cd, S, and Cu elements in CdS/Cu. Subsequently, Pt cocatalyst is deposited onto the surface of CdS/Cu NSs to construct CdS/Cu/Pt composites *via* a photochemical reduction method.[44] The actual weight ratios of Cu and Pt have been tested by inductively coupled plasma optical emission spectrometry (**Table S1**). As can be seen from **Figure 1b**, **S2a** and **S2b**, no Pt NPs are observed on CdS/Cu/Pt composite, which exhibits well-maintained lamellar morphology and preserves lattice fringes with d-spacing of 0.34 and 0.36 nm, suggesting atomically dispersed Pt on CdS/Cu/Pt. The EDX spectrum (**Figure S2c**) and elemental mapping results (**Figure S2d**) demonstrate the homogeneous dispersion of Pt on CdS/Cu NSs. Aberration-corrected high-angle annular dark field scanning TEM (HAADF-STEM) has been implemented to identify the configuration of Pt species on CdS/Cu/Pt. As delineated in **Figure 1c**, the individually isolated bright dots marked by white circles unveil the existence of Pt single atoms (SAs) on CdS/Cu/Pt. In the line profile from the blue line in **Figure 1c**, a maximum peak corresponding to the individual Pt atom is observed, further confirming the presence of Pt SAs (**Figure S2e**).
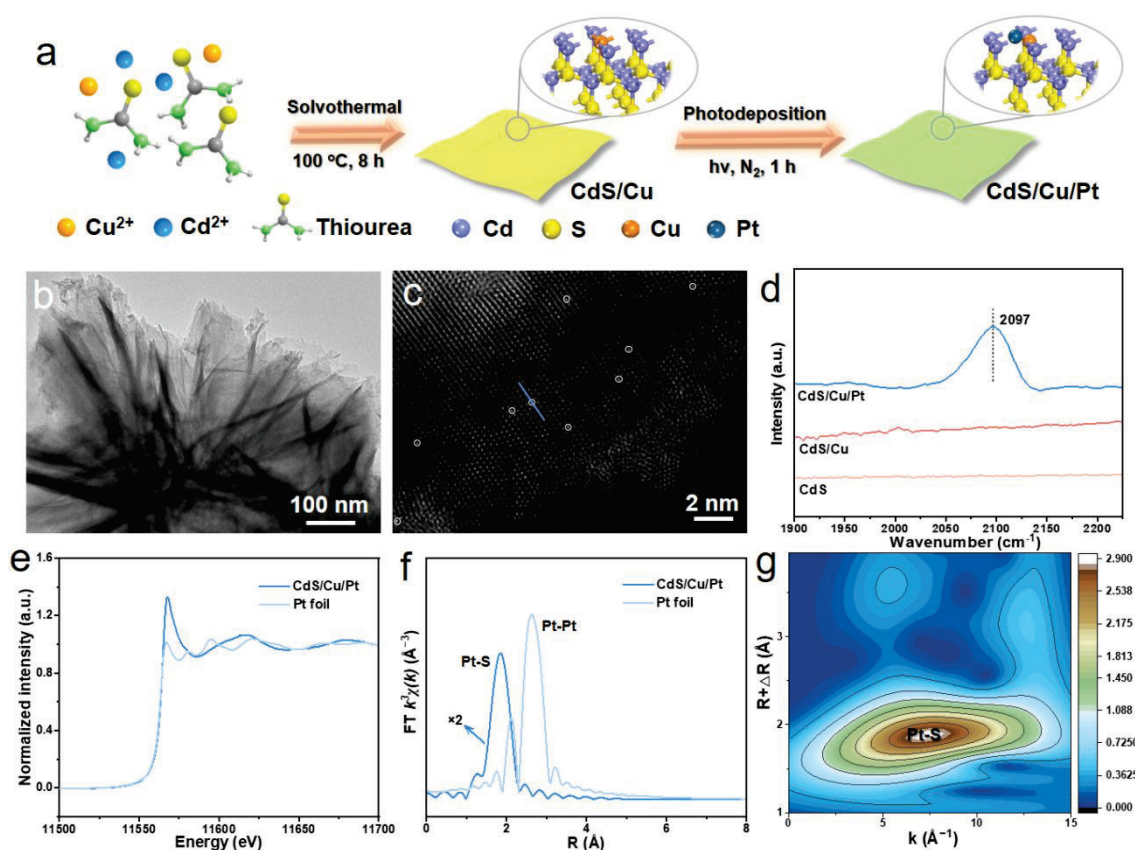
Figure 1. (a) The flowchart of the fabrication of CdS/Cu/Pt composite. (b) TEM and (c) aberration-corrected HAADF-STEM image of CdS/Cu/Pt composite. (d) FT-IR spectra of adsorbed CO on as-prepared samples after desorption process. (e) Pt L_3-edge XANES and (f) FT-EXAFS spectra of CdS/Cu/Pt and Pt foil. (g) The WT of k_2-weighted EXAFS spectra of CdS/Cu/Pt.

The carbon monoxide (CO) adsorption behavior on as-prepared samples has been inspected by Fourier-transform infrared (FT-IR) spectroscopy to identify metal SAs.[25,45] As mirrored in **Figure 1d**, upon purging with argon (Ar) at 25 °C for 10 minutes to remove gaseous and weakly adsorbed CO, no CO adsorption band appears in the FT-IR spectra of CdS and CdS/Cu. In the FT-IR spectrum of CdS/Cu/Pt, only a vibration band centered at 2097 cm^{-1} is detected, which is assigned to the linear adsorption of CO on Pt$^{\delta+}$ sites, indicating atomically dispersed Pt atoms on CdS/Cu/Pt.[46] For the purpose of uncovering the coordination environment of Pt species in CdS/Cu/Pt, X-ray absorption spectroscopy (XAS) has been performed. As shown in **Figure 1e**, the Pt L_3-edge X-ray absorption near-edge structure (XANES) spectrum of CdS/Cu/Pt exhibits a different spectrum shape in comparison with that of Pt foil, ruling out the presence of Pt-Pt bonds in CdS/Cu/Pt.[30,47] The higher white-line intensity and threshold energy of CdS/Cu/Pt than those of Pt foil reveal the oxidation state of Pt, which is attributed to the Pt-S coordination mode in CdS/Cu/Pt.[27] Quantitative coordination configuration of Pt in CdS/Cu/Pt has been revealed by Fourier transform extended X-ray absorption fine structure (FT-EXAFS) curve fitting with reference to Pt foil (**Figure 1f**, **S3a** and **S3b** for

4

R-spaces, **Figure S3c-e** for K-spaces). FT-EXAFS spectrum of CdS/Cu/Pt displays only one prominent peak assignable to the Pt-S bond at *ca.* 1.9 Å without any Pt-Pt contribution at 2.6 Å, testifying the atomically dispersed Pt in CdS/Cu/Pt.[48] As exhibited in **Table S2**, the Pt-S coordination number (CN) in CdS/Cu/Pt is 4.2 ± 0.3, elucidating that one Pt atom is bonded to four S atoms to construct a Pt_1-S_4 coordination structure in CdS/Cu/Pt. In order to visually reflect the coordination information of Pt species in CdS/Cu/Pt, wavelet transform (WT) for k_2-weighted EXAFS spectra have been performed in the resolution of R-space and K-space (**Figure 1g** and **S3f**). The WT contour plot of CdS/Cu/Pt exhibits a maximum intensity at 1.9 Å in R-space and 6.9 $Å^{-1}$ in K-space, corresponding to the Pt-S bond in the first coordination shell, further corroborating the sole presence of Pt SAs in CdS/Cu/Pt.[27]

X-ray photoelectron spectroscopy (XPS) has been performed to study the surface chemical states and electron transfer pathway of catalysts. As observed in the high-resolution Cd 3d XPS spectra of bare CdS (**Figure 2a**), the peaks at binding energies of 410.7 and 403.9 eV correspond to Cd $3d_{3/2}$ and Cd $3d_{5/2}$, which are associated with Cd^{2+} in CdS.[49] The S 2p XPS spectra (**Figure 2b**) of CdS are deconvoluted into S $2p_{1/2}$ (161.4 eV) and S $2p_{3/2}$ (160.5 eV), corresponding to the S^{2-} in CdS.[50] It is worth noting that the binding energies of Cd 3d and S 2p in the CdS/Cu hybrid are positively shifted in comparison with those in bare CdS, revealing the role of Cd and S as electron donors in CdS/Cu, as well as the strong interaction between CdS and Cu dopant.[51] Compared with the Cd 3d and S 2p XPS spectra of CdS/Cu, a positive binding energy shift is found in the Cd 3d and S 2p XPS spectra of CdS/Cu/Pt, indicating the transport of photoexcited electrons from CdS/Cu to Pt SAs.[52] As delineated in **Figure 2c**, the Cu 2p XPS spectra of CdS/Cu show $2p_{1/2}$ and $2p_{3/2}$ doublets at 953.0 and 933.2 eV, which are ascribed to Cu^{2+}.[53] By contrast, the binding energies of Cu 2p in CdS/Cu/Pt negatively shift in comparison with those of CdS/Cu, further corroborating the photoelectron transfer from CdS/Cu to Pt SAs. As depicted in **Figure 2d**, the Pt 4f spectra of CdS/Cu/Pt exhibit two peaks at binding energies of 72.0 and 75.5 eV, respectively, originating from Pt $4f_{7/2}$ and $4f_{5/2}$ peaks for $Pt^{\delta+}$, which is consistent with XANES results.[27]

For the purpose of further investigating the valence state of Cu dopant and vacancy properties of the catalysts, low-temperature electron paramagnetic resonance (EPR) spectroscopy has been performed. As shown in **Figure 2e**, no discernable signal appears in the EPR spectrum of bare CdS, while CdS/Cu and CdS/Cu/Pt display the characteristic signals with a g value of 2.08, which are ascribed to Cu^{2+}.[53-55] Furthermore, the EPR spectrum of bare CdS exhibits a typical signal of sulfur vacancy at g = 2.003. The intensities of EPR peaks assignable to sulfur vacancy over CdS/Cu and CdS/Cu/Pt are stronger than that over CdS, indicating that the doping of Cu promotes the formation of sulfur vacancy (**Figure S5**).[20,56] Raman spectra have also been conducted to identify the doping form of Cu in CdS. As shown in **Figure 2f**, Raman peaks of blank CdS are situated at 298 and 593 cm^{-1}, which are the characteristic features of the first- and second-order longitudinal optical (LO) modes, respectively.[50]
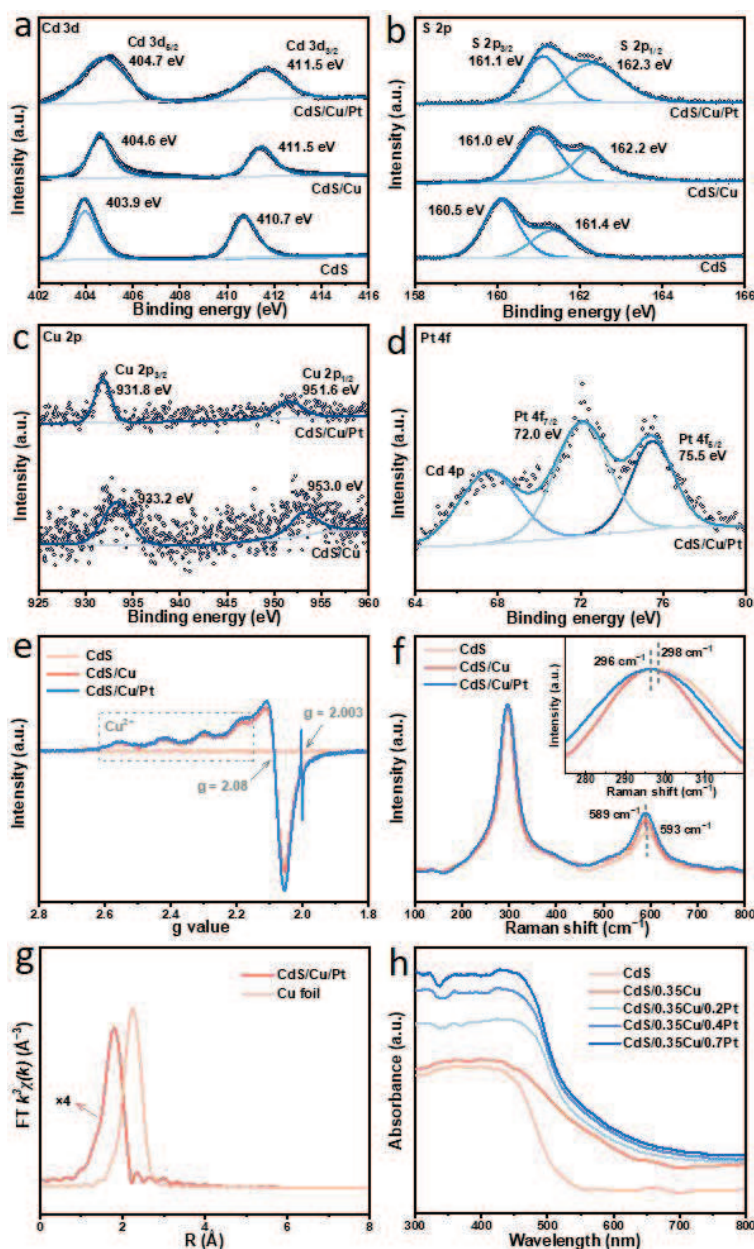
5

Figure 2. XPS spectra of (a) Cd 3d and (b) S 2p for CdS, CdS/Cu, and CdS/Cu/Pt. XPS spectra of (c) Cu 2p for CdS/Cu and CdS/Cu/Pt. XPS spectra of (d) Pt 4f for CdS/Cu/Pt. (e) Low-temperature EPR spectra and (f) Raman spectra of CdS, CdS/Cu, and CdS/Cu/Pt. (g) FT-EXAFS spectra of CdS/Cu/Pt and Cu foil. (h) DRS spectra of CdS, CdS/0.35Cu, and CdS/Cu/xPt composites.

After introducing Cu into CdS, the Raman peaks of CdS/Cu slightly shift towards the lower wavenumber, and the peak of CuS situated around 473 nm is not detected, indicating that Cu is successfully doped into the CdS lattice instead of forming CuS, which is further validated by X-ray diffraction (XRD) patterns of CdS/Cu composites (**Figure S6a**).[57-59] Compared to CdS/Cu, the shift of Raman peaks of CdS/Cu/Pt is not found, proving that the surface structure of CdS/Cu is not changed by the photodeposition of Pt. In addition, XAS has been conducted to determine the

6

coordination structure of Cu dopant in CdS/Cu/Pt. The XANES spectra of CdS/Cu/Pt and Cu foil (**Figure S7a**) demonstrate the oxidation state of Cu dopant. As displayed in the FT-EXAFS spectra (**Figure 2g**, **S7b** and **S7c**), a prominent peak at *ca.* 1.8 Å assigned to the Cu-S bond is detected, while the typical Cu-Cu contribution is absent, indicating the substitution of Cu for Cd in CdS NSs.[25,55]

The ultraviolet–visible (UV–vis) diffuse reflectance spectra (DRS) have been used to measure the optical absorption information of as-synthesized samples. As displayed in **Figure S8a**, blank CdS possesses an intrinsic band gap absorption edge at *ca.* 520 nm.[17] CdS/Cu hybrids exhibit an absorption tail in the visible region, as well as gradually enhanced light absorption with the increase of Cu content, implying that the doping of Cu has a significant impact on the visible light absorption of CdS.[22] According to the Tauc plots in **Figure S8b**, the calculated band gap of CdS/Cu (2.35 eV) is slightly smaller than that of bare CdS (2.55 eV).[22] The conduction band minimums of CdS and CdS/Cu are respectively estimated according to the Mott-Schottky analysis (**Figure S8c**) and their band structures are displayed in **Figure S8d**. Furthermore, with the addition of Pt, the light absorption of CdS/Cu/Pt composites is slightly enhanced in the visible region(**Figure 2h**).[60]

Taking benzylamine (BA) as a model substrate, the photocatalytic performance of as-prepared samples toward BA dehydrocoupling and H_2 generation has been assayed under visible light ($\lambda >$ 420 nm) illumination and Ar atmosphere (**Figure 3a**). As shown in **Figure 3b** and **S9a**, bare CdS shows relatively low H_2 production (373 μmol g^{-1} h^{-1}) and BA conversion (6.0 %) with 47.8% selectivity to N-benzylbenzaldimine (BBAD) and 52.2% selectivity to saturated product dibenzylamine (DBA). After doping Cu into CdS, the photoactivities of CdS/Cu composites are elevated and CdS/0.35Cu exhibits the highest BA conversion (33.8%), which is 4.6 times higher than that of bare CdS. The major liquid product turns into DBA and H_2 production is reduced, because the transformation of BBAD to DBA undergoes a hydrogenation process.[13,61,62] The subsequent deposition of Pt onto CdS/Cu not only enhances the BA conversion and H_2 production, which exhibit a volcano-type trend, but also adjusts the selectivity of BA dehydrocoupling from DBA to BBAD.[12] The optimal BBAD and H_2 production rates of 4611 and 4723 μmol g^{-1} h^{-1} are achieved over CdS/Cu/0.4Pt with a BBAD selectivity of above 99%. The molar ratios of H_2 and BBAD yields are calculated to be approximately 1.0, signifying a stoichiometric photoredox dehydrogenative coupling reaction.[10] In contrast, the photoactivities of CdS/Pt composites are evaluated and the optimal BBAD and H_2 production rates over CdS/0.4Pt are lower than those of CdS/Cu/Pt composites, elucidating the considerable contribution of Cu dopant to the boosted photoactivity over CdS/Cu/Pt composites (**Figure S9b**). As depicted in **Figure 3c**, the yields of BBAD and H_2 increase with the prolonged illumination time, giving a BA conversion of up to 94.8% over CdS/Cu/0.4Pt after 2 h of light illumination. As depicted in **Figure 3d**, apparent quantum yields (AQYs) of H_2 over CdS/Cu/0.4Pt under different monochromatic lights are dependent on the wavelength of incident light and consistent with the DRS spectrum of CdS/Cu/0.4Pt composite, manifesting that this photoredox dehydrocoupling reaction is driven by the light excitation of CdS. In comparison with previous literatures for photocatalytic dehydrocoupling of amines, our present work possesses relatively good performance, as illustrated in **Table S4**. Moreover, we performed a gram-scale reaction to evaluate the scalability of photocatalytic synthesis of BBAD by BA dehydrocoupling and 1.12 g (85.4% yield) of BBAD has been obtained over CdS/Cu/0.4Pt within 20 h.
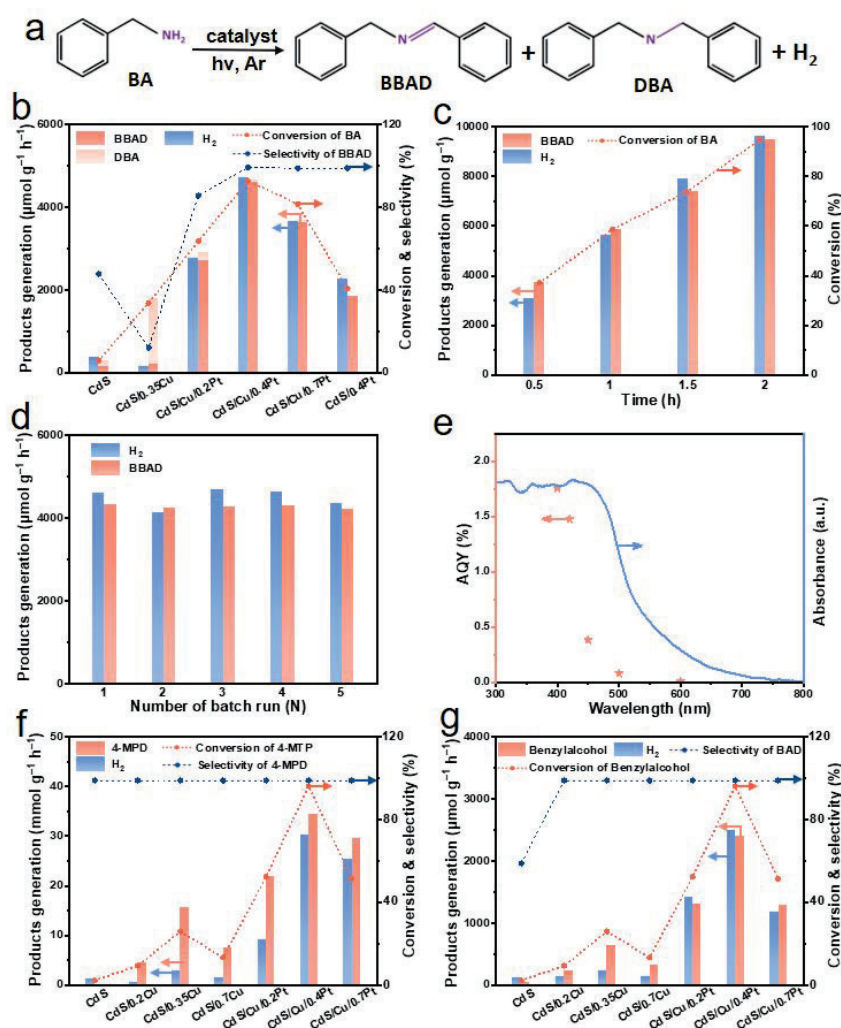
Figure 3. (a) Reaction scheme for cooperative photocatalytic BA dehydrocoupling and H_2 evolution. (b) Photocatalytic performance of BA dehydrocoupling integrated with H_2 evolution over as-prepared samples under visible light illumination for 2 h. (c) Time profiles of BBAD and H_2 production over CdS/Cu/0.4Pt. (d) DRS spectrum and AQY for H_2 evolution over CdS/Cu/0.4Pt under different monochromatic lights. (e) Recycling tests of CdS/Cu/0.4Pt. (f) Photocatalytic performance of 4-MTP dehydrocoupling integrated with H_2 evolution over as-prepared samples under visible light illumination for 0.5 h. (g) Photocatalytic performance of benzyl alcohol oxidation integrated with H_2 evolution over as-prepared samples under visible light illumination for 4 h.

For the sake of assessing the stability of CdS/Cu/Pt composite, reusability tests have been implemented. As can be seen in **Figure 3e**, no obvious photoactivity loss is observed after 5 cycles of 10 h, manifesting the favorable photocatalytic stability of CdS/Cu/Pt. Furthermore, the morphology, crystallographic structure, and chemical valence of CdS/Cu/Pt show negligible change after reusability tests, further evidencing its good stability for photoredox-catalyzed BA dehydrocoupling (**Figure S10a-c** and **S11a-e**).

8

The general applicability of CdS/Cu/Pt composite for dehydrocoupling of amines integrated with H_2 evolution has also been examined by using a variety of primary amines with different substituent groups and heteroatom-containing amines as substrates. As shown in **Table 1**, **entries 1-6**, the primary amines with electron-donating groups (e.g., methyl group, methoxy group, and dimethoxy group) or electron-withdrawing groups (e.g., –F and –Cl) on the aryl ring are converted into the corresponding imines with high yield and selectivity. This system is also compatible with heterocyclic primary amines with O and S moieties to deliver the corresponding products, although the reaction time needs to be extended (**Table 1**, **entries 7** and **8**). Based on above analysis, CdS/Cu/Pt composite possesses good substrate tolerance for the dual-functional photoredox-system for amines conversion and H_2 production. Furthermore, photocatalytic thiols conversion coupled with H_2 evolution and benzyl alcohol oxidation paired with H_2 production reactions have been adopted as probe reactions to verify the generality of atomic-level Cu-Pt electron transfer channel strategy for improving the performance of photoredox reactions.[63] As shown in **Figure 3f**, upon visible light irradiation for 0.5 h, CdS/Cu composites present enhanced photoactivities for concurrent production of bis(4-methoxyphenyl) disulfide (4-MPD) and H_2 from the dehydrocoupling of 4-methoxythiophenol (4-MTP) in comparison with that of bare CdS. The conversion of 4-MTP over optimal CdS/0.35Cu composite improves from 2.2% to 26.0%. After the immobilization of Pt SAs, CdS/Cu/Pt composites exhibit higher photocatalytic performance than CdS/Cu composites, and the conversion of 4-MTP over optimal CdS/Cu/0.4Pt achieves 96.2% along with the H_2 production rate of 30.3 mmol g^{-1} h^{-1}. As shown in **Figure 3g**, the introduction of Cu dopants and Pt SAs synergistically promotes the activity of photocatalytic benzyl alcohol oxidation coupled with H_2 evolution, which is in conformity to above trend of 4-MTP dehydrocoupling activity. In summary, these results suggest the promising scope of using atomic-level Cu-Pt electron transfer channel strategy to improve the photoredox-catalyzed performance of various organic synthesis reactions.

Table 1. Substrate scope of photocatalytic amines dehydrocoupling and H_2 evolution using CdS/Cu/0.4Pt.[a]

Entry	Amine substrate	Yield of liquid product (μmol)	Yield of H_2 (μmol)	Time (h)
1			42.8	44.2	2
2			49.7	49.1	2
3			49.1	47.8	2
4			48.9	41.4	2

Entry	Amine	Imine			
5			49.7	43.5	2
6			47.2	47.7	2
7			43.1	46.7	6
8			42.6	45.0	6

[a] Reaction conditions: 5 mg of CdS/Cu/0.4Pt, 0.1 mmol of primary amines, 5 mL of acetonitrile, Ar atmosphere, visible light ($\lambda > 420$ nm).

With the view of shedding light on the effect of introducing Cu dopant and Pt SAs on the enhanced photocatalytic performance, (photo)electrochemical tests and photoluminescence (PL) experiments have been performed to investigate the charge carrier dynamics. The transient photocurrent responses of samples have been tested under intermittent visible light irradiation (**Figure 4a**). Compared with bare CdS, CdS/Cu possesses increased photocurrent density, revealing the higher separation efficiency of photogenerated charge carriers. When Pt SAs are loaded on CdS/Cu, the photocurrent density of CdS/Cu/Pt further enhances, which is attributed to the role of Pt as an electron trap, as well as the combined synergy between Cu dopant and Pt SAs.[18,25] As illustrated in **Figure 4b**, electrochemical impedance spectroscopy (EIS) plot of CdS/Cu/Pt possesses a smaller arc at high frequency than CdS/Cu and bare CdS, revealing that more efficient electron transport and lower charge transfer resistance between CdS/Cu/Pt and electrolyte are acquired than those over CdS/Cu and bare CdS.[17,64] Mott-Schottky analysis has been used to provide quantitative insights into the charge carrier densities (N_D) of CdS, CdS/Cu, and CdS/Cu/Pt, which are calculated to be 3.30×10^{15}, 3.64×10^{15}, and 3.94×10^{15} cm^{-3}, respectively, manifesting the enhanced charge transfer over CdS/Cu/Pt in comparison with CdS/Cu and CdS (**Figure S12a**).[65,66] As evidenced by linear-sweep voltammograms (LSV) in **Figure 4c**, the doping of Cu and incorporation of Pt SAs result in decreased overpotential of proton reduction over CdS/Cu/Pt as compared to CdS/Cu and CdS.[17,49]

Furthermore, PL and time-resolved PL (TRPL) spectra, which are widely used to explore the fate of photoinduced electrons and holes have been performed to validate above deduction. The PL spectra measured under 405 nm monochromatic light excitation are depicted in **Figure 4d**. In comparison with CdS, the PL intensity of CdS/Cu diminishes, while the PL signal of CdS/Cu/Pt is almost quenched, revealing that the recombination of photoexcited charge carriers in CdS/Cu/Pt is remarkably suppressed compared to those of CdS and CdS/Cu.[67,68] The TRPL spectra and fitting results (**Figure S12b** and **Table S5**) also identify that the introduction of Cu dopant and Pt SAs facilitates the electron transfer in CdS/Cu/Pt composite.[25,69]
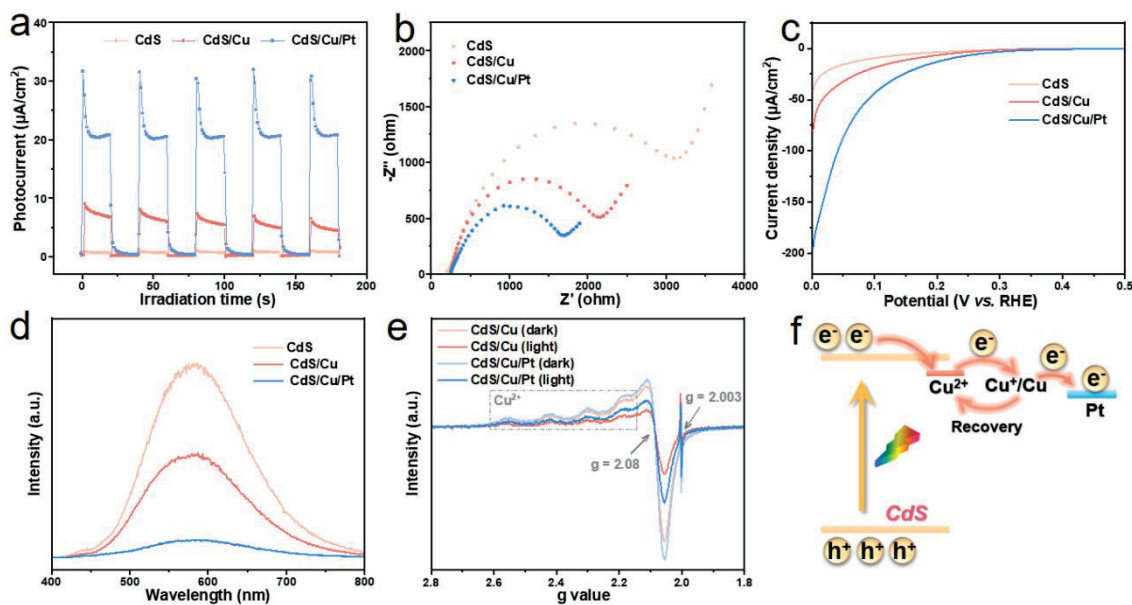
Figure 4. (a) Transient photocurrent responses, (b) EIS Nyquist plots, (c) LSV curves, and (d) PL spectra (λ_{ex} = 405 nm) of CdS, CdS/Cu and CdS/Cu/Pt. (e) In situ low-temperature EPR spectra of CdS/Cu and CdS/Cu/Pt under dark or light illumination. (f) Schematic diagram of Cu-Pt electron transfer channel in CdS/Cu/Pt.

To obtain direct insight into the charge transfer pathway in CdS/Cu/Pt, in situ low-temperature EPR spectra have been collected. As displayed in **Figure 4e**, upon 10 minutes of light irradiation, the intensity of characteristic signal assigned to Cu^{2+} over CdS/Cu decreases, which is due to the reduction of Cu^{2+} to EPR-silent Cu^{+}/Cu^{0} by trapping photoelectrons from CdS.[54,55] As for CdS/Cu/Pt, the decrease of signal intensity is weaker than that of CdS/Cu, which is attributed to the electron transfer from Cu^{+}/Cu^{0} to Pt SAs, implying that Cu dopant serves as a unique electron bridge to construct a directional Cu-Pt electron transfer channel with the assistance of Pt SAs (**Figure 4f**).[55,70] As depicted in **Figure S13a-c**, the Cu^{2+} signals over CdS/Cu and CdS/Cu/Pt gradually disappear as the light illumination time extends to 30 minutes. After exposing CdS/Cu and CdS/Cu/Pt to oxygen atmosphere in the dark, the characteristic signal of Cu^{2+} reappears, unveiling the recovery of diamagnetic Cu^{+}/Cu^{0} back to paramagnetic Cu^{2+}.[55]

With the purpose of investigating the variations of reactants and products in photocatalytic BA dehydrocoupling over obtained samples, in situ FT-IR spectroscopy has been carried out. As displayed in the in situ FT-IR spectra of CdS/Cu/Pt (**Figure 5a**), the peaks at 3297 and 3378 cm^{-1} with decreased intensity correspond to the stretching vibration of N–H bond in BA, unveiling the consumption of BA under visible light illumination.[13] The peaks at 1453 and 1496 cm^{-1} are in agreement with the stretching vibration of C=C bonds in benzene ring.[8] With the extension of illumination time, another peak with ever-increasing intensity is detected at 1644 cm^{-1}, which is assigned to the C=N bond in BBAD, uncovering the gradual formation of BBAD.[8,13] Notably, in the FT-IR spectra of bare CdS and CdS/Cu (**Figure S14a** and **b**), the intensity of peaks at 1644 cm^{-1} first increases and then decreases, disclosing that BBAD first forms and then converts to DBA under visible light illumination. Since DBA is produced through the hydrogenation process of BBAD, and
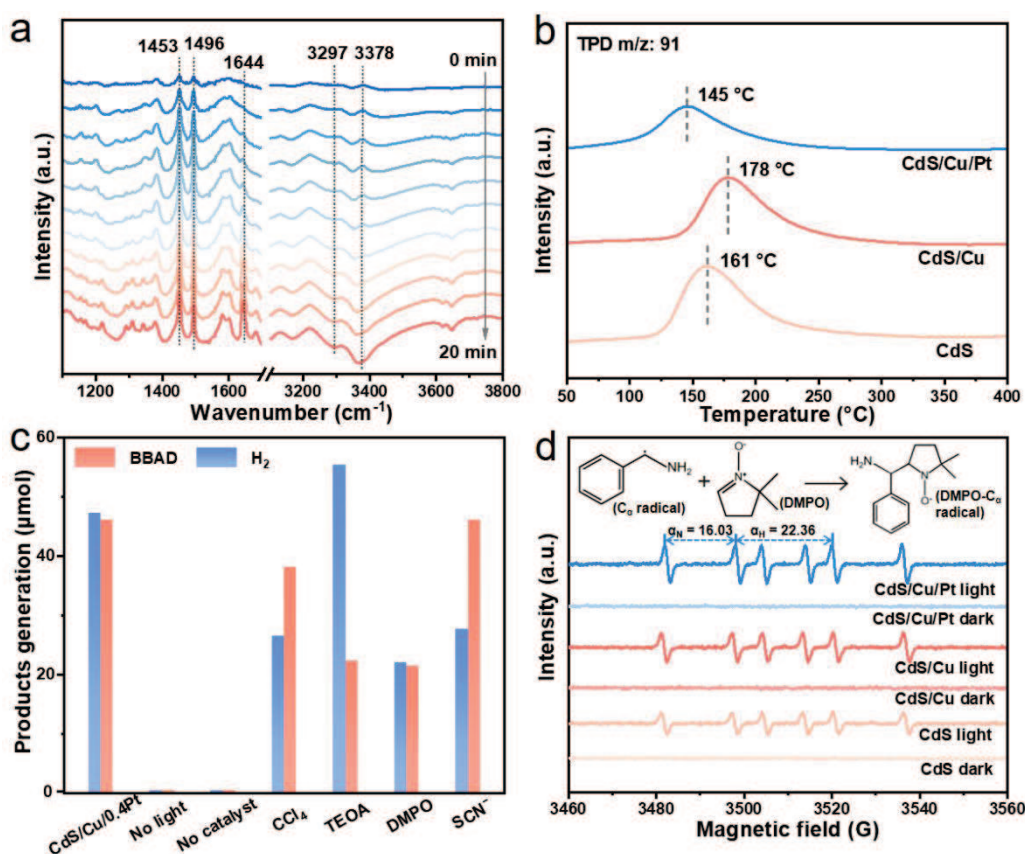
11

Figure 5. (a) In situ FT-IR spectra of photocatalytic BA dehydrocoupling over CdS/Cu/Pt. (b) TPD analysis of BBAD adsorption on CdS, CdS/Cu, and CdS/Cu/Pt. (c) Control experiments with different conditions catalyzed by CdS/Cu/Pt. (d) DMPO spin-trapping EPR spectra over CdS, CdS/Cu, and CdS/Cu/Pt in BA solution with or without visible light illumination.

Cu-based catalysts are beneficial to the hydrogenation reactions,[13,61,62] the adsorption of BBAD on the as-prepared samples is presumed to be an important parameter affecting the product selectivity of photocatalytic BA dehydrocoupling system. To corroborate this hypothesis, the interaction of BBAD with as-prepared samples has been investigated by the temperature programmed desorption (TPD) characterization (**Figure 5b**). Compared with the desorption peak of BBAD at 161 °C for CdS, the single peak of BBAD desorption for CdS/Cu is detected at 178 °C, disclosing that the doping of Cu enhances the interaction between BBAD and CdS/Cu, which is conducive to the conversion of BBAD to DBA through the hydrogenation reaction. As for CdS/Cu/Pt, the desorption peak of BBAD at reduced temperature (145 °C) demonstrates the relatively weak adsorption of BBAD on CdS/Cu/Pt. The introduction of Pt SAs decreases the overpotential of proton reduction and adsorption of BBAD over CdS/Cu/Pt, thus contributing to its high selectivity of BBAD.[12]

To gain more insights into the photocatalytic mechanism for cooperative H_2 evolution and BA dehydrocoupling, a series of control experiments have been conducted to detect the reactive species.

12

As shown in **Figure 5c**, no BBAD or H_2 are detected without light or photocatalyst, revealing that the dehydrocoupling of BA is a photo-driven process.[18] The addition of carbon tetrachloride (CCl_4)
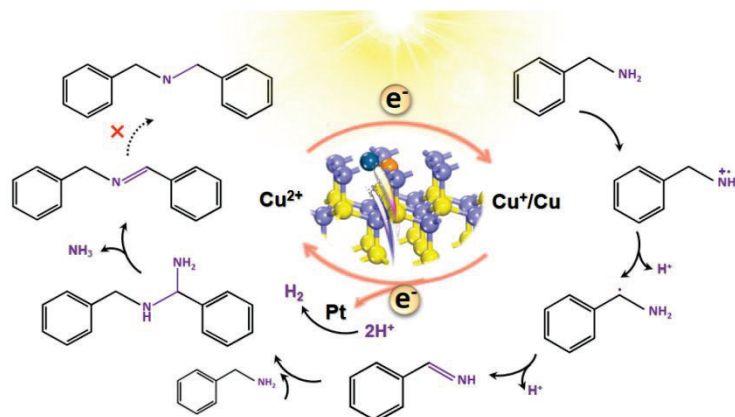

Figure 6. Proposed photocatalytic mechanism over CdS/Cu/Pt.

as an electron scavenger or triethanolamine (TEOA) as a hole scavenger respectively restrains the generation of H_2 or BBAD, demonstrating the synchronous utilization of electrons and holes for H_2 formation and BA dehydrocoupling.[49] When 5,5-dimethyl-1-pyrroline N-oxide (DMPO) is added into this photoredox-catalyzed system to trap radicals, the decreased yield of H_2 and BBAD suggests the crucial role of free radicals in this reaction.[68] To delve deep into the role of Pt SAs in BA dehydrocoupling reaction, we have executed a control experiment with the addition of thiocyanate ion (SCN^-), which is widely used to poison Pt cocatalysts.[71] After adding SCN^- into the reaction system, the production of H_2 is severely restrained, while the production of BBAD is almost unchanged, demonstrating the dominant contribution of Pt SAs as catalytic sites for H_2 production in BA dehydrocoupling reaction.[25] This is consistent with the LSV tests, in which the decoration of Pt SAs obviously reduces the overpotential of H_2 evolution.

The EPR technique using DMPO as a trapping agent has been implemented to obtain more information on active radical intermediates produced in this reaction (**Figure 5d**). In the dark, spin-adduct signals cannot be discovered. After 5 minutes of light illumination, six characteristic peaks indexed to the DMPO-Ph($\cdot$CH)NH_2 adducts are observed, the nitrogen hyperfine splitting (α_N) and hydrogen hyperfine splitting (α_H) of which are respectively calculated to be 16.03 and 22.36 G.[13] The intensity of EPR peaks of CdS/Cu/Pt is higher than those of CdS/Cu and bare CdS, which is in line with their photoactivity trend, elucidating that the doping of Cu and deposition of Pt synergistically promote the deprotonation of BA to Ph($\cdot$CH)NH_2 radicals, thus accelerating the production of BBAD and H_2. In addition, as displayed in **Figure S15** and **S16a-c**, the mass spectrum and UV-vis absorption spectra respectively demonstrate the generation of Ph(CH)NH intermediate and NH_3 during the photocatalytic BA dehydrocoupling reaction over CdS/Cu/Pt.

In light of the aforementioned analyses, a potential mechanism for photo-driven dehydrocoupling of BA integrated with H_2 generation over CdS/Cu/Pt is proposed (**Figure 6**). After CdS is excited by

13

visible light, the electrons in the conduction band of CdS are trapped by Cu^{2+} dopant, which is simultaneously reduced to Cu^+/Cu^0. Then, Pt SAs act as the electron sink to extract electrons from Cu^+/Cu^0 *via* the directional Cu-Pt charge transfer channel, while Cu^+/Cu^0 is re-oxidized to Cu^{2+} for continuous capture of electrons from CdS. The electrons accumulated on Pt SAs are used for reducing the protons released from BA oxidation to H_2. Meanwhile, the holes stored in the valence band of CdS oxidize the α-C−H bond of BA adsorbed on CdS/Cu/Pt to release proton and generate a Ph(•CH)NH$_2$ radical intermediate, which is subsequently deprotonated to generate a highly active Ph(CH)NH intermediate. According to the addition-elimination mechanism, the Ph(CH)NH intermediate is coupled with another BA molecule to synthesize N-benzyl-1-phenylmethanediamine, which is converted to C−N coupled BBAD along with the release of NH_3. Because of the weak adsorption of BBAD on Pt SAs, the above synthesized BBAD does not undergo the undesirable hydrogenation reaction to form DBA, resulting in the high selectivity of BBAD over CdS/Cu/Pt.

3. Conclusion

To sum up, we report the efficient and selective cooperative photoredox of H_2 production and dehydrogenative C−N coupling of amines into imines with good substrate tolerance over CdS/Cu/Pt composite. Mechanistic studies reveal that Cu dopant acts as a unique electron bridge to fabricate a directional Cu-Pt electron transfer channel at atomic-level by capturing electrons from CdS NSs and then releasing them to Pt SAs, during which the doped Cu^{2+} undergoes the reduction to Cu^+/Cu^0 and recovery to Cu^{2+}, thereby accelerating the transfer kinetics of photoinduced charge carriers. Pt SAs play a dual role in increasing the H_2 evolution and improving the selectivity of imines by taking advantages of decreased overpotential of proton reduction and weak adsorption of imines on Pt. Furthermore, a thorough investigation of active species and intermediates in the photocatalytic process reveals the underlying addition-elimination mechanism for BA dehydrocoupling. This research is expected to pave the way for the elaborate design of highly-active atomic photocatalysts for the selective synthesis of high-value chemical feedstocks coupled with H_2 generation.

4. Experimental Section

Synthesis of CdS NSs. CdS NSs were synthesized through a modified solvothermal method.[42] Firstly, 1 mmol Cd(CH$_3$COO)$_2$·2H$_2$O and 3 mmol SC(NH$_2$)$_2$ were evenly dispersed in a mixture of 28 mL ethylenediamine and 1.5 mL DI water by stirring for 30 minutes. Secondly, the transparent mixed solution was transferred to a 50 mL Teflon-line autoclave and heated at 100 °C for 8 h. Lastly, the resulting slurry was centrifuged, rinsed with DI water 4 times and dried in a vacuum oven at 60 °C.

Synthesis of CdS/xCu NSs. The fabrication of CdS/Cu NSs was implemented as above solvothermal method, except for adding the calculated amount of Cu(CH$_3$COO)$_2$·H$_2$O.[43] The obtained CdS/xCu NSs with different weight ratios of Cu dopant (0.2%, 0.35%, and 0.7%) were labeled as CdS/0.2Cu, CdS/0.35Cu, and CdS/0.7Cu, respectively.

Synthesis of CdS/Cu/xPt composites. The facile photodeposition method was employed to prepare CdS/Cu/Pt composites.[44] Typically, 40 mg of CdS/0.35Cu NSs powder and a calculated amount of H$_2$PtCl$_6$ were dispersed in 40 mL of mixed solution (v (CH$_3$CH$_2$OH)/v (H$_2$O) = 1:4) to form a

homogeneous yellow suspension. After bubbling in nitrogen (N_2) atmosphere (flow rate = 40 mL min^{-1}) for 20 minutes, the suspension was illuminated by a 300 W Xe arc lamp ($\lambda > 420$ nm, PLS-SXE 300D, Beijing Perfectlight Co., Ltd.) for 1 h under N_2 atmosphere. Then, the sediment was collected by filtration, washed with DI water, and finally dried in a vacuum oven at 60 °C. The prepared CdS/Cu/xPt composites with different weight ratios of Pt (0.2%, 0.4%, and 0.7%) were labeled as CdS/Cu/0.2Pt, CdS/Cu/0.4Pt, and CdS/Cu/0.7Pt, respectively.

Photocatalytic tests. The photoactivity tests for the cooperative BA conversion and H_2 evolution were conducted in a double-walled quartz reactor equipped with a condensate water circulation system, which was used to keep the photocatalytic reaction at 25 °C. Typically, 5 mg photocatalyst and 0.1 mmol BA were dispersed into 5 mL acetonitrile *via* ultrasonication for 5 minutes. After that, the suspension was purged with Ar gas (flow rate = 40 mL min^{-1}) for 20 minutes and illuminated by a 300 W Xe arc lamp ($\lambda > 420$ nm, PLS-SXE 300D, Beijing Perfectlight Co., Ltd.) for 2 h. The light power density of the Xe arc lamp was tested as 400 mW cm^{-2} by a photoradiometer (PL-MW2000, Beijing Perfectlight Co., Ltd.). After irradiation, the suspension was filtered by an organic needle filter with a pore size of 0.22 μm to obtain a clarified reaction solution, which was analyzed by a gas chromatograph-mass spectrometer (Shimadzu GC-MS QP 2020, Q-Exactive, see **Figure S17** for corresponding Mass spectra). The yield of H_2 was analyzed by a gas chromatograph (Shimadzu GC-2014C, 13X column, Ar carrier) equipped with a thermal conductivity detector (TCD).

AUTHOR INFORMATION

Corresponding Author

Zi-Rong Tang – College of Chemistry, State Key Laboratory of Photocatalysis on Energy and Environment, Fuzhou University, Fuzhou 350116, P. R. China; orcid.org/0000-0002-6564-3539; Email: zrtang@fzu.edu.cn

Yi-Jun Xu – College of Chemistry, State Key Laboratory of Photocatalysis on Energy and Environment, Fuzhou University, Fuzhou 350116, P. R. China; orcid.org/0000-0002-2195-1695; Email: yjxu@fzu.edu.cn; http:// xugroup.fzu.edu.cn

Authors

Yue-Hua Li – College of Chemistry, State Key Laboratory of Photocatalysis on Energy and Environment, Fuzhou University, Fuzhou 350116, P. R. China

Yin-Feng Wang – College of Chemistry, State Key Laboratory of Photocatalysis on Energy and Environment, Fuzhou University, Fuzhou 350116, P. R. China

Jing-Yu Li – College of Chemistry, State Key Laboratory of Photocatalysis on Energy and Environment, Fuzhou University, Fuzhou 350116, P. R. China

Ming-Yu Qi – College of Chemistry, State Key Laboratory of Photocatalysis on Energy and Environment, Fuzhou University, Fuzhou 350116, P. R. China

Marco Conte – Department of Chemistry, University of Sheffield, Sheffield, S3 7HF, (UK)

Author Contributions

All authors have given approval to the final version of the manuscript.

Notes

Any additional relevant notes should be placed here.

ASSOCIATED CONTENT

Supporting Information

The Supporting Information is available free of charge at https://pubs.acs.org/doi/10.1021/acscatal.xxxxxxx.

Additional experimental details, characterizations and photoactivity results. Energy band structure of obtained samples. UV-vis absorption spectrum for ammonium production. Mass spectra of reactant and obtained liquid-products. (PDF)

ACKNOWLEDGMENT

REFERENCES

(1) Zhang, B.; Guo, X.-W.; Liang, H.; Ge, H.; Gu, X.; Chen, S.; Yang, H.; Qin, Y. Tailoring Pt–Fe$_2$O$_3$ Interfaces for Selective Reductive Coupling Reaction To Synthesize Imine. *ACS Catal.* **2016**, *6*, 6560-6566.

(2) Liu, H.; Xu, C.; Li, D.; Jiang, H.-L. Photocatalytic Hydrogen Production Coupled with Selective Benzylamine Oxidation over MOF Composites. *Angew. Chem. Int. Ed.* **2018**, *57*, 5379-5383.

(3) Bories, C.C.; Barbazanges, M.; Derat, E.; Petit, M. Implication of a Silyl Cobalt Dihydride Complex as a Useful Catalyst for the Hydrosilylation of Imines. *ACS Catal.* **2021**, *11*, 14262-14273.

(4) Lv, D.; Li, Y.; Qiao, W.; Zhang, D.; Mai, Y.; Cai, N.; Xiang, H.; Li, Y.; Niemantsverdriet, H.; Hao, W.; Su, R. Metal cocatalyst mediated photocatalytic dehydrogenative-condensation and direct condensation cross-coupling of aniline and alcohol. *Appl. Catal., B* **2022**, *309*, 121264.

(5) Qi, M.-Y.; Conte, M.; Anpo, M.; Tang, Z.-R.; Xu, Y.-J. Cooperative Coupling of Oxidative Organic Synthesis and Hydrogen Production over Semiconductor-Based Photocatalysts. *Chem. Rev.* **2021**, *121*, 13051-13085.

(6) Shang, R.; Zhang, Q.; Lin, P.; Gu, B.; Tang, Q.; Cao, Q.; Fang, W. Aerobic activation of alcohols on Zn-promoted atomically-dispersed Ru sites encapsulated within UiO-66 framework for imine synthesis. *Appl. Catal., B* **2022**, *319*, 121904.

(7) Sun, D.; Ye, L.; Li, Z. Visible-light-assisted aerobic photocatalytic oxidation of amines to imines over NH$_2$-MIL-125(Ti). *Appl. Catal., B* **2015**, *164*, 428-432.

(8) Wei, S.; Zhong, H.; Wang, H.; Song, Y.; Jia, C.; Anpo, M.; Wu, L. Oxygen vacancy enhanced visible light photocatalytic selective oxidation of benzylamine over ultrathin Pd/BiOCl nanosheets. *Appl. Catal., B* **2022**, *305*, 121032.

(9) Han, C.; Li, Y.-H.; Li, J.-Y.; Qi, M.-Y.; Tang, Z.-R.; Xu, Y.-J. Cooperative Syngas Production and C−N Bond Formation in One Photoredox Cycle. *Angew. Chem. Int. Ed.* **2021**, *60*, 7962-7970.

(10) Qi, M.-Y.; Conte, M.; Tang, Z.-R.; Xu, Y.-J. Engineering Semiconductor Quantum Dots for Selectivity Switch on High-Performance Heterogeneous Coupling Photosynthesis. *ACS Nano* **2022**, *16*, 17444-17453.

(11) Liu, W.; Wang, Y.; Huang, H.; Wang, J.; He, G.; Feng, J.; Yu, T.; Li, Z.; Zou, Z. Spatial Decoupling of Redox Chemistry for Efficient and Highly Selective Amine Photoconversion to Imines. *J. Am. Chem. Soc.* **2023**, *145*, 7181-7189.

(12) Yu, J.; Liu, Q.; Qiao, W.; Lv, D.; Li, Y.; Liu, C.; Yu, Y.; Li, Y.; Niemantsverdriet, H.; Zhang, B.; Su, R. Catalytic Role of Metal Nanoparticles in Selectivity Control over Photodehydrogenative Coupling of Primary Amines to Imines and Secondary Amines. *ACS Catal.* **2021**, *11*, 6656-6661.

(13) Zheng, J.-H.; Qi, M.-Y.; Tang, Z.-R.; Xu, Y.-J. Manipulating selective amine transformation pathways via cocatalyst-modified monolayer $ZnIn_2S_4$ photocatalysts. *J. Mater. Chem. A* **2023**, *11*, 4013-4019.

(14) Li, J.-Y.; Li, Y.-H.; Qi, M.-Y.; Lin, Q.; Tang, Z.-R.; Xu, Y.-J. Selective Organic Transformations over Cadmium Sulfide-Based Photocatalysts. *ACS Catal.* **2020**, *10*, 6262-6280.

(15) Yu, W.; Zhang, D.; Guo, X.; Song, C.; Zhao, Z. Enhanced visible light photocatalytic non-oxygen coupling of amines to imines integrated with hydrogen production over Ni/CdS nanoparticles. *Catal. Sci. Technol.* **2018**, *8*, 5148-5154.

(16) Bie, C.; Zhu, B.; Wang, L.; Yu, H.; Jiang, C.; Chen, T.; Yu, J. A Bifunctional $CdS/MoO_2/MoS_2$ Catalyst Enhances Photocatalytic H_2 Evolution and Pyruvic Acid Synthesis. *Angew. Chem. Int. Ed.* **2022**, *61*, e202212045.

(17) Li, Y.-H.; Qi, M.-Y.; Li, J.-Y.; Tang, Z.-R.; Xu, Y.-J. Noble metal free $CdS@CuS-Ni_xP$ hybrid with modulated charge transfer for enhanced photocatalytic performance. *Appl. Catal., B* **2019**, *257*, 117934.

(18) Li, J.-Y.; Li, Y.-H.; Zhang, F.; Tang, Z.-R.; Xu, Y.-J. Visible-Light-Driven Integrated Organic Synthesis and Hydrogen Evolution over 1D/2D $CdS-Ti_3C_2T_x$ MXene Composites. *Appl. Catal., B* **2020**, *269*, 118783.

(19) Pradhan, N.; Das Adhikari, S.; Nag, A.; Sarma, D.D. Luminescence, Plasmonic, and Magnetic Properties of Doped Semiconductor Nanocrystals. *Angew. Chem. Int. Ed.* **2017**, *56*, 7038-7054.

(20) Liu, Y.; Zhou, Y.; Zhou, X.; Jin, X.; Li, B.; Liu, J.; Chen, G. Cu doped SnS_2 nanostructure induced sulfur vacancy towards boosted photocatalytic hydrogen evolution. *Chem. Eng. J.* **2021**, *407*, 127180.

(21) Shi, R.; Ye, H.-F.; Liang, F.; Wang, Z.; Li, K.; Weng, Y.; Lin, Z.; Fu, W.-F.; Che, C.-M.; Chen, Y. Interstitial P-Doped CdS with Long-Lived Photogenerated Electrons for Photocatalytic Water Splitting without Sacrificial Agents. *Adv. Mater.* **2018**, *30*, 1705941.

(22) Wang, Y.; Yang, X.; Ye, T.; Xu, C.; Xia, F.; Meng, D. Comparative Study of Structural and Photocatalytic Properties of M-Doped (M = Ce^{3+}, Zn^{2+}, Cu^{2+}) Dendritic-Like CdS. *J. Electron. Mater.* **2017**, *46*, 1598-1606.

(23) Lei, B.; Cui, W.; Chen, P.; Chen, L.; Li, J.; Dong, F. C–Doping Induced Oxygen-Vacancy in WO_3 Nanosheets for CO_2 Activation and Photoreduction. *ACS Catal.* **2022**, *12*, 9670-9678.

(24) Chen, F.; Ma, T.; Zhang, T.; Zhang, Y.; Huang, H. Atomic-Level Charge Separation Strategies in Semiconductor-Based Photocatalysts. *Adv. Mater.* **2021**, *33*, 2005256.

(25) Su, L.; Wang, P.; Wang, J.; Zhang, D.; Wang, H.; Li, Y.; Zhan, S.; Gong, J. Pt–Cu Interaction Induced Construction of Single Pt Sites for Synchronous Electron Capture and Transfer in Photocatalysis. *Adv. Funct. Mater.* **2021**, *31*, 2104343.

(26) Sun, C.; Zhang, H.; Liu, H.; Zheng, X.; Zou, W.; Dong, L.; Qi, L. Enhanced activity of visible-light photocatalytic H_2 evolution of sulfur-doped g-C_3N_4 photocatalyst via nanoparticle metal Ni as cocatalyst. *Appl. Catal., B* **2018**, *235*, 66-74.

(27) Shi, X.; Dai, C.; Wang, X.; Hu, J.; Zhang, J.; Zheng, L.; Mao, L.; Zheng, H.; Zhu, M. Protruding Pt single-sites on hexagonal $ZnIn_2S_4$ to accelerate photocatalytic hydrogen evolution. *Nat. Commun.* **2022**, *13*, 1287.

(28) Liu, L.; Corma, A. Metal Catalysts for Heterogeneous Catalysis: From Single Atoms to Nanoclusters and Nanoparticles. *Chem. Rev.* **2018**, *118*, 4981-5079.

(29) Luo, L.; Fu, L.; Liu, H.; Xu, Y.; Xing, J.; Chang, C.-R.; Yang, D.-Y.; Tang, J. Synergy of Pd atoms and oxygen vacancies on In_2O_3 for methane conversion under visible light. *Nat. Commun.* **2022**, *13*, 2930.

(30) Shi, X.; Huang, Y.; Bo, Y.; Duan, D.; Wang, Z.; Cao, J.; Zhu, G.; Ho, W.; Wang, L.; Huang, T.; Xiong, Y. Highly Selective Photocatalytic CO_2 Methanation with Water Vapor on Single-Atom Platinum-Decorated Defective Carbon Nitride. *Angew. Chem. Int. Ed.* **2022**, *61*, e202203063.

(31) Liu, X.; Hao, Z.; Wang, H.; Wang, T.; Shen, Z.; Zhang, H.; Zhan, S.; Gong, J. Enhanced localized dipole of Pt-Au single-site catalyst for solar water splitting. *Proc. Natl. Acad. Sci. U.S.A.* **2022**, *119*, e2119723119.

(32) Liu, J.; Zou, Y.; Cruz, D.; Savateev, A.; Antonietti, M.; Vilé, G. Ligand-Metal Charge Transfer Induced via Adjustment of Textural Properties Controls the Performance of Single-Atom Catalysts during Photocatalytic Degradation. *ACS Appl. Mater. Interfaces* **2021**, *13*, 25858-25867.

(33) Gawande, M.B.; Fornasiero, P.; Zbořil, R. Carbon-Based Single-Atom Catalysts for Advanced Applications. *ACS Catal.* **2020**, *10*, 2231-2259.

(34) Bakandritsos, A.; Kadam, R.G.; Kumar, P.; Zoppellaro, G.; Medved, M.; Tuček, J.; Montini, T.; Tomanec, O.; Andrýsková, P.; Drahoš, B.; Varma, R.S.; Otyepka, M.; Gawande, M.B.; Fornasiero, P.; Zbořil, R. Mixed-Valence Single-Atom Catalyst Derived from Functionalized Graphene. *Adv. Mater.* **2019**, *31*, 1900323.

(35) Pieta, I.S.; Kadam, R.G.; Pieta, P.; Mrdenovic, D.; Nowakowski, R.; Bakandritsos, A.; Tomanec, O.; Petr, M.; Otyepka, M.; Kostecki, R.; Khan, M.A.M.; Zboril, R.; Gawande, M.B. The Hallmarks of Copper Single Atom Catalysts in Direct Alcohol Fuel Cells and Electrochemical CO_2 Fixation. *Adv. Mater. Interfaces* **2021**, *8*, 2001822.

(36) Liu, D.; Wan, X.; Kong, T.; Han, W.; Xiong, Y. Single-atom-based catalysts for photoelectrocatalysis: challenges and opportunities. *J. Mater. Chem. A* **2022**, *10*, 5878-5888.

(37) Gawande, M.B.; Ariga, K.; Yamauchi, Y. Single-Atom Catalysts. *Small* **2021**, *17*, 2101584.

(38) Shen, Y.; Ren, C.; Zheng, L.; Xu, X.; Long, R.; Zhang, W.; Yang, Y.; Zhang, Y.; Yao, Y.; Chi, H.; Wang, J.; Shen, Q.; Xiong, Y.; Zou, Z.; Zhou, Y. Room-temperature photosynthesis of propane from CO_2 with Cu single atoms on vacancy-rich TiO_2. *Nat. Commun.* **2023**, *14*, 1117.

(39) Dong, X.a.; Cui, Z.; Shi, X.; Yan, P.; Wang, Z.; Co, A.C.; Dong, F. Insights into Dynamic Surface Bromide Sites in $Bi_4O_5Br_2$ for Sustainable N_2 Photofixation. *Angew. Chem. Int. Ed.* **2022**, *61*, e202200937.

(40) Wu, X.; Zhang, Q.; Li, W.; Qiao, B.; Ma, D.; Wang, S.L. Atomic-Scale Pd on 2D Titania Sheets for Selective Oxidation of Methane to Methanol. *ACS Catal.* **2021**, *11*, 14038-14046.

(41) Yan, J.; Wang, T.; Wu, G.; Dai, W.; Guan, N.; Li, L.; Gong, J. Tungsten Oxide Single Crystal Nanosheets for Enhanced Multichannel Solar Light Harvesting. *Adv. Mater.* **2015**, *27*, 1580-1586.

(42) Song, S.; Qu, J.; Han, P.; Hülsey, M.J.; Zhang, G.; Wang, Y.; Wang, S.; Chen, D.; Lu, J.; Yan, N. Visible-light-driven amino acids production from biomass-based feedstocks over ultrathin CdS nanosheets. *Nat. Commun.* **2020**, *11*, 4899.

(43) He, B.; Liu, R.; Ren, J.; Tang, C.; Zhong, Y.; Hu, Y. One-Step Solvothermal Synthesis of Petalous Carbon-Coated Cu^+-Doped CdS Nanocomposites with Enhanced Photocatalytic Hydrogen Production. *Langmuir* **2017**, *33*, 6719-6726.

(44) Qi, M.-Y.; Li, Y.-H.; Zhang, F.; Tang, Z.-R.; Xiong, Y.; Xu, Y.-J. Switching Light for Site-Directed Spatial Loading of Cocatalysts onto Heterojunction Photocatalysts with Boosted Redox Catalysis. *ACS Catal.* **2020**, *10*, 3194-3202.

(45) Wang, T.; Tao, X.; Li, X.; Zhang, K.; Liu, S.; Li, B. Synergistic Pd Single Atoms, Clusters, and Oxygen Vacancies on TiO_2 for Photocatalytic Hydrogen Evolution Coupled with Selective Organic Oxidation. *Small* **2021**, *17*, 2006255.

(46) Fang, X.; Shang, Q.; Wang, Y.; Jiao, L.; Yao, T.; Li, Y.; Zhang, Q.; Luo, Y.; Jiang, H.-L. Single Pt Atoms Confined into a Metal–Organic Framework for Efficient Photocatalysis. *Adv. Mater.* **2018**, *30*, 1705112.

(47) Qiu, S.; Shen, Y.; Wei, G.; Yao, S.; Xi, W.; Shu, M.; Si, R.; Zhang, M.; Zhu, J.; An, C. Carbon dots decorated ultrathin CdS nanosheets enabling in-situ anchored Pt single atoms: A highly efficient solar-driven photocatalyst for hydrogen evolution. *Appl. Catal., B* **2019**, *259*, 118036.

(48) Wu, Y.; Wu, Q.; Zhang, Q.; Lou, Z.; Liu, K.; Ma, Y.; Wang, Z.; Zheng, Z.; Cheng, H.; Liu, Y.; Dai, Y.; Huang, B.; Wang, P. An organometal halide perovskite supported Pt single-atom photocatalyst for H_2 evolution. *Energy Environ. Sci.* **2022**, *15*, 1271-1281.

(49) Li, Y.-H.; Zhang, F.; Chen, Y.; Li, J.-Y.; Xu, Y.-J. Photoredox-catalyzed biomass intermediate conversion integrated with H_2 production over $Ti_3C_2T_x$/CdS composites. *Green Chem.* **2020**, *22*, 163-169.

(50) Xu, J.; Cao, X. Characterization and mechanism of MoS_2/CdS composite photocatalyst used for hydrogen production from water splitting under visible light. *Chem. Eng. J.* **2015**, *260*, 642-648.

(51) Zhang, B.; Chen, C.; Liu, J.; Qiao, W.; Zhao, J.; Yang, J.; Yu, Y.; Chen, S.; Qin, Y. Simultaneous Ni nanoparticles decoration and Ni doping of CdS nanorods for synergistically promoting photocatalytic H_2 evolution. *Appl. Surf. Sci.* **2020**, *508*, 144869.

(52) Ning, X.; Wu, Y.; Ma, X.; Zhang, Z.; Gao, R.; Chen, J.; Shan, D.; Lu, X. A Novel Charge Transfer Channel to Simultaneously Enhance Photocatalytic Water Splitting Activity and Stability of CdS. *Adv. Funct. Mater.* **2019**, *29*, 1902992.

19

(53) Nosaka, Y.; Takahashi, S.; Sakamoto, H.; Nosaka, A.Y. Reaction Mechanism of Cu(II)-Grafted Visible-Light Responsive TiO_2 and WO_3 Photocatalysts Studied by Means of ESR Spectroscopy and Chemiluminescence Photometry. *J. Phys. Chem. C* **2011**, *115*, 21283-21290.

(54) Yuan, L.; Hung, S.-F.; Tang, Z.-R.; Chen, H.M.; Xiong, Y.; Xu, Y.-J. Dynamic Evolution of Atomically Dispersed Cu Species for CO_2 Photoreduction to Solar Fuels. *ACS Catal.* **2019**, *9*, 4824-4833.

(55) Wang, G.; Wu, Y.; Li, Z.; Lou, Z.; Chen, Q.; Li, Y.; Wang, D.; Mao, J. Engineering a Copper Single-Atom Electron Bridge to Achieve Efficient Photocatalytic CO_2 Conversion. *Angew. Chem. Int. Ed.* **2023**, *62*, e202218460.

(56) Tan, Y.-X.; Chai, Z.-M.; Wang, B.-H.; Tian, S.; Deng, X.-X.; Bai, Z.-J.; Chen, L.; Shen, S.; Guo, J.-K.; Cai, M.-Q.; Au, C.-T.; Yin, S.-F. Boosted Photocatalytic Oxidation of Toluene into Benzaldehyde on $CdIn_2S_4$-CdS: Synergetic Effect of Compact Heterojunction and S-Vacancy. *ACS Catal.* **2021**, *11*, 2492-2503.

(57) Dai, X.; Chen, L.; Li, Z.; Li, X.; Wang, J.; Hu, X.; Zhao, L.; Jia, Y.; Sun, S.-X.; Wu, Y.; He, Y. $CuS/KTa_{0.75}Nb_{0.25}O_3$ nanocomposite utilizing solar and mechanical energy for catalytic N_2 fixation. *J. Colloid Interface Sci.* **2021**, *603*, 220-232.

(58) Hu, X.-S.; Shen, Y.; Zhang, Y.-T.; Zhang, H.-F.; Xu, L.-H.; Xing, Y.-J. Synthesis of flower-like CuS/reduced graphene oxide (RGO) composites with significantly enhanced photocatalytic performance. *J. Alloys Compd.* **2017**, *695*, 1778-1785.

(59) Aftab, F.; Iqbal, J.; Iqbal, A.; Mahmood, A.; Raza, Q. Effect of Cu incorporation on the physical properties of CdS thin films deposited by using the thermal evaporation technique. *J. Korean Phys. Soc.* **2016**, *69*, 593-597.

(60) Chen, Y.; Ji, S.; Sun, W.; Lei, Y.; Wang, Q.; Li, A.; Chen, W.; Zhou, G.; Zhang, Z.; Wang, Y.; Zheng, L.; Zhang, Q.; Gu, L.; Han, X.; Wang, D.; Li, Y. Engineering the Atomic Interface with Single Platinum Atoms for Enhanced Photocatalytic Hydrogen Production. *Angew. Chem. Int. Ed.* **2020**, *59*, 1295-1301.

(61) Wang, B.; Cui, Y.; Wen, C.; Chen, X.; Dong, Y.; Dai, W.-L. Role of copper content and calcination temperature in the structural evolution and catalytic performance of Cu/P25 catalysts in the selective hydrogenation of dimethyl oxalate. *Appl. Catal., A* **2016**, *509*, 66-74.

(62) Kominami, H.; Higa, M.; Nojima, T.; Ito, T.; Nakanishi, K.; Hashimoto, K.; Imamura, K. Copper-Modified Titanium Dioxide: A Simple Photocatalyst for the Chemoselective and Diastereoselective Hydrogenation of Alkynes to Alkenes under Additive-Free Conditions. *ChemCatChem* **2016**, *8*, 2019-2022.

(63) Sportelli, G.; Boselli, T.; Protti, S.; Serpone, N.; Ravelli, D. Photovoltaic Materials as Heterogeneous Photocatalysts: A Golden Opportunity for Sustainable Organic Syntheses. *Sol. RRL* **2023**, *7*, 2201008.

(64) Wang, Y.-F.; Qi, M.-Y.; Conte, M.; Tang, Z.-R.; Xu, Y.-J. New Radical Route and Insight for the Highly Efficient Synthesis of Benzimidazoles Integrated with Hydrogen Evolution. *Angew. Chem. Int. Ed.* **2023**, *62*, e202304306.

(65) Zhang, N.; Qi, M.-Y.; Yuan, L.; Fu, X.; Tang, Z.-R.; Gong, J.; Xu, Y.-J. Broadband Light Harvesting and Unidirectional Electron Flow for Efficient Electron Accumulation for Hydrogen Generation. *Angew. Chem. Int. Ed.* **2019**, *58*, 10003-10007.

20

(66) Wang, G.; Wang, Q.; Lu, W.; Li, J. Photoelectrochemical Study on Charge Transfer Properties of TiO_2-B Nanowires with an Application as Humidity Sensors. *J. Phys. Chem. B* **2006**, *110*, 22029-22034.

(67) Li, X.; Wang, J.; Wang, H.; Wang, B.; Li, Y.-Y.; Xu, J.; Tian, M.; Lin, H.; Wang, L. CoP-Embedded Graphitic N-Doped C Nanosheets in Ohmic Contact with S-Deficient CdS Nanocrystals Triggering Efficient Visible-Light Photocatalytic H_2 Evolution. *ACS Appl. Nano Mater.* **2023**, *6*, 4437-4448.

(68) Qi, M.-Y.; Lin, Q.; Tang, Z.-R.; Xu, Y.-J. Photoredox coupling of benzyl alcohol oxidation with CO_2 reduction over CdS/TiO_2 heterostructure under visible light irradiation. *Appl. Catal., B* **2022**, *307*, 121158.

(69) Liu, Y.; Zhu, Q.; Tayyab, M.; Zhou, L.; Lei, J.; Zhang, J. Single-Atom Pt Loaded Zinc Vacancies ZnO–ZnS Induced Type-V Electron Transport for Efficiency Photocatalytic H_2 Evolution. *Sol. RRL* **2021**, *5*, 2100536.

(70) Wang, H.; Qi, H.; Sun, X.; Jia, S.; Li, X.; Miao, T.J.; Xiong, L.; Wang, S.; Zhang, X.; Liu, X.; Wang, A.; Zhang, T.; Huang, W.; Tang, J. High quantum efficiency of hydrogen production from methanol aqueous solution with $PtCu–TiO_2$ photocatalysts. *Nat. Mater.* **2023**, *22*, 619-626.

(71) Liang, H.-W.; Brüller, S.; Dong, R.; Zhang, J.; Feng, X.; Müllen, K. Molecular metal–N_x centres in porous carbon for electrocatalytic hydrogen evolution. *Nat. Commun.* **2015**, *6*, 7992.

TOC GRAPHICS

Atomic-level Cu-Pt
Electron Transfer Channel

22